Online Grid Impedance Estimation-Based Adaptive Control of VSGs Considering Strong and Weak Grid Conditions

Online Grid Impedance Estimation-Based Adaptive Control of VSGs Considering Strong and Weak Grid Conditions

Nabil Mohammed, *Member, IEEE*, Mohammad Hasan Ravanji, *Member, IEEE*, Weihua Zhou, *Member, IEEE*, and Behrooz Bahrani, *Senior Member, IEEE*

***Abstract*—The conventional virtual synchronous generator (VSG) is normally designed to meet certain operational and control requirements in the islanded mode. However, once the VSG is switched to grid-connected mode (GCM), the robust operation cannot be guaranteed under different grid conditions. It can lead to, especially in strong grids, poor dynamic performance such as significant oscillation, long settling time, and high overshoot. In order to improve the VSG performance in the GCM, this article first analyzes in depth the inherent coupling between the active and reactive power and its dependence on the grid conditions, such as the short circuit ratio, grid impedance ratio $X_{\rm g}/R_{\rm g}$, and the wide grid impedance variations. Afterwards, an online grid impedance estimation-based adaptive VSG (AVSG) control strategy is proposed to ensure the robust operation of the VSG considering both strong and weak grid conditions. This technique allows the operator to specify the desired settling time of output power and damping ratio.To estimate the grid impedance in real time without extra hardware and reduce the associated impacts on power quality, an online event-based grid impedance estimation algorithm is embedded into the control loop of the AVSG. Both the simulation and experimental results indicate that, compared to the conventional fixed-parameters-based controller design method, the AVSG enables the desired performance such as no oscillation, specified time duration for the settling time, and minimal overshoot regardless of the grid conditions.**

***Index Terms*—Adaptive control, online grid impedance estimation, stability, strong grid, virtual synchronous generator, weak grid.**

I. Introduction

RECENTLY, renewable energies such as wind and solar power have been explored and used in the worldwide due to the fossil fuel shortage, environmental pollution, and global temperature rise [1]. Different from the conventional synchronous generator-interfaced hydraulic and thermal power generations, these renewable energies are mainly connected to the utility grid via the highly controllable, flexible, and efficient power electronic converters [2]. In spite of these remarkable advantages, these converters currently in service rely mainly on the phase-locked loop (PLL) for grid synchronization in order to inject specified power or current command, which may induce control interaction-related instability phenomena or limit the maximum power transfer capability under weak grid conditions [3]–[5]. It is thus desirable to eliminate the usage of the PLL in these converter interfaces, which leads to increasing research interests in both academia and industry for the emerging PLL-less grid-forming technology [6].

This work has been supported by the Monash Grid Innovation Hub and the Australian Renewable Energy Agency (ARENA) under the Advancing Renewable Program (Grant No.: 2020/ARP007) (*Corresponding author: Nabil Mohammed*).

The authors are with the Department of Electrical and Computer Systems Engineering, Monash University, 3800 Victoria, Australia (e-mail: nabil.mohammed@ieee.org; mohammad.ravanji@monash.edu; weihua.zhou@monash.edu; behrooz.bahrani@monash.edu).

Various kinds of grid-forming control strategies have been developed in the existing literature, e.g., droop control, power synchronization control, virtual synchronous generator (VSG), synchronverter, matching control, virtual oscillator control [7]. Among them, the VSG has been regarded as a promising key technology for achieving the 100% inverter-interfaced renewable grid, since it enables these power electronic converters to mimic both the steady-state and transient-state characteristics of the conventional synchronous generators. The VSG not only accurately tracks the power command but also provides inertia and damping to the utility grid [8].

The VSG can operate in the islanded mode (IM) as well as in the grid-connected mode (GCM). On the one hand, the main task of the VSG in the IM is to form the microgrid voltage and frequency, the rotor inertia and damping at least by a one of the inverter especially in the absence of the conventional synchronous generators. On the other hand, the main task of the VSG in the GCM is to inject the active power specified by its reference value, while the terminal voltage and frequency are regulated by the utility grid [9]. The integration of large-scale wind and solar farms located at remote sites can make these integration areas electrically weak due to the long transmission lines connection [10]. The conventional grid-following control strategies cannot provide the adequate inertia support for the grid under this circumstance, which may impose the risk of instability for the more renewable-energy-integrated power system [11]. The voltage, frequency, and inertia support in these grid-connected regions using the grid-forming concept is thus in the strong need.

Although many research studies have been conducted to improve the VSG control performance, there are still some challenges under investigation [8]. Among them, the coupling between the active and reactive power output that can lead to the stability and dynamic performance degradation of the power system and the reactive power absorption increase to provide the active power support [12]. Furthermore, the severe power coupling results in transient oscillations and even instability operation [13]. The decoupling between the active and reactive power is only satisfied in high-or medium-voltage grids where the grid impedance ratio $X_{\rm g}/R_{\rm g}$ is large enough such that the line impedance could be regarded as mainly inductive [14], [15]. However, the power coupling exists in a low-voltage grid due to the small $X_{\rm g}/R_{\rm g}$ ratio of line impedance, i.e., any change of the active power output will affect the reactive power output, vice versa [11].

Considering the above-mentioned issues, it is important to analyze the negative impacts of the grid impedance on the power coupling of grid-forming inverters. However, most of the control strategies in the literature that address the power coupling issues focus only on the droop-based grid-forming

inverters. These techniques include virtual inductance [16], virtual impedance [17], adaptive virtual impedance [18], adaptive droop control [19], and various improved droop control strategies [20]. Few studies focus on addressing the power coupling issues in the VSG-based grid-forming inverters, especially in GCM. In [21], the power equations considering a resistive-inductive grid impedance are linearized at a specific operating point. Then, a power decoupling method based on compensating for the coupling components of the power equations is presented. In [13], to assess the power coupling characteristics, a unified dynamic power coupling model is presented. In [11], the limitation of using only virtual inductance to decouple the power flow is investigated. Then, a q-axis voltage-drop-based power decoupling control is proposed. Furthermore, the effects of adopting the virtual inductance on power decoupling are assessed in detail in [22]. In [9], a generalized control is presented to meet the operation requirements in both the GCM and IM. Hence, in the GCM, the oscillations are suppressed and the settling time of output power are reduced.

Despite the above efforts to eliminate the power decoupling issue in the VSG-based grid-forming inverters, several shortcomings remain to be resolved. First, the control design proposed based on linearization and decoupling, e.g., in [21], is valid and accurate only for the specific linearized operating point. Second, the proposed control design, e.g., in [19], [23], assume the grid impedance is purely inductive, which is not the case in weak and low voltage grids. Last but not least, there is no comprehensive study that reveals the VSG performance in the GCM considering operating scenarios with different short circuit ratio (SCR) values, different grid impedance ratios $X_{\mathrm{g}}/R_{\mathrm{g}}$ and grid impedance variations with the same $X_{\mathrm{g}}/R_{\mathrm{g}}$ ratio.

This paper initially presents a comprehensive study to reveal the VSG performance in the GCM under different grid impedance conditions, i.e., different SCR, different $X_{\mathrm{g}}/R_{\mathrm{g}}$ ratios, and different grid impedance amplitudes. Then, an adaptive VSG (AVSG) control strategy is proposed to eliminate the negative impacts of the grid impedance on the power coupling between the active and reactive power loops regardless the grid conditions. The advantages of the proposed control is summarized as follows:

1) It relies on online estimation of the grid equivalent model (i.e., resistance and inductance) in order to adaptively tune the VSG parameters. Hence, it can stably operate in both weak and strong grids.
2) To avoid practical complications caused by using network analyzers for impedance estimation purposes, an online event-based active grid impedance estimation (GIE) technique is embedded into the control of the AVSGs. It only utilizes the available PCC voltage and current measurements to estimate the grid impedance components accurately.
3) It ensures full decoupling and control of the active and reactive powers with the same desired dynamic performance such as no oscillation, specified time duration for the settling time, and minimal overshoot.

The rest of this paper is organized as follows. Section II provides a comprehensive review on the conventional VSG including the control structure, the performance in the IM, the performance in the GCM, and a summary of the remaining challenges related to grid parameters (e.g., SCR and X/R ratios) that hinder accurate control of VSG-based inverters in the GCM. Section III describes the proposed AVSG. Section IV presents simulation and experimental results. Finally, Section V draws the conclusions.

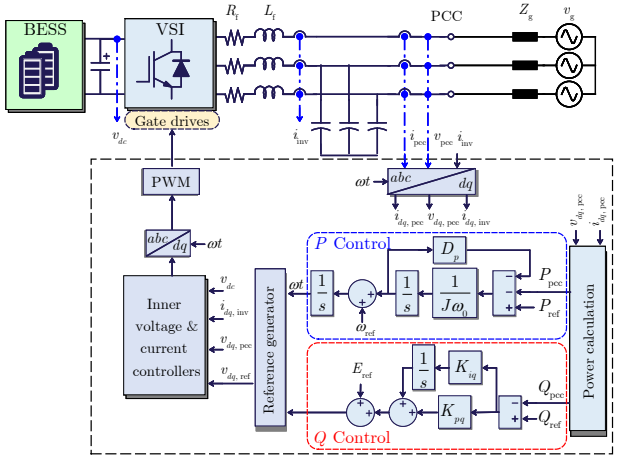

Fig. 1: Control structure of a conventional VSG-based grid-forming inverter.

II. Control of the Conventional VSG

A. Control Structure of the Conventional VSG

Fig. 1 shows the topology and control diagram of a conventional VSG-based grid-forming inverter. The inverter is connected via an L filter (with an inductance L_{f} and equivelent series resistance R_{f}) to the grid or load (not shown in the figure). The utility grid is modelled using the Thevenin equivalent circuit that consists of the grid voltage source (V_{g}) and the grid impedance ($Z_{\mathrm{g}} = R_{\mathrm{g}} + sL_{\mathrm{g}}$).

Here, fixed values are normally assigned for the virtual damping D_p and the virtual inertia J at the design stage by considering the operation requirements in the IM. Although the designed fixed values for the VSGs parameters can still perform better in weak grids, they are prone to induce poor transient response with high overshoot and long-time oscillations in strong grids that have relatively small grid impedances [7]. Therefore, the performance of the VSGs is highly dependent on the grid conditions, as will be illustrated below.

B. Control of the Conventional VSG in the IM

In the IM, the VSG is expected to provide frequency support when the load changes. Hence, the inertia and damping parameters of the VSG are designed to meet the rate of change of frequency (ROCOF) requirements. In Fig. 1, by neglecting the line losses, the small-signal transfer function from the load variation ΔP_{load} to the angular frequency variation $\Delta\omega$ can be derived as

$$\frac{\Delta\omega}{\Delta P_{\mathrm{load}}} = -\frac{1}{J\omega_0 s + D_p}, \tag{1}$$

where ω_0, D_p, and J are the grid nominal angular frequency, the damping coefficient, and the inertia coefficient of the VSG, respectively. Eq. (1) can be rearranged as

$$\frac{\Delta\omega}{\Delta P_{\mathrm{load}}} = -\frac{1}{D_p}\frac{1}{\frac{J\omega_0}{D_p}s + 1}. \tag{2}$$

Assuming that $T_{\mathrm{VSG}} = \frac{J\omega_0}{D_p}$ is the time constant of the VSG, (2) can be rewritten as

$$\Delta\omega = -\frac{1}{D_p}\frac{1}{T_{\mathrm{VSG}}s + 1}\Delta P_{\mathrm{load}}. \tag{3}$$

T_{VSG} is related to the desired initial ROCOF. The ROCOF requirement varies in different countries. For example, the

ROCOF requirement in Ireland is 0.5 Hz/s. In Australia, the Australian National Electricity Rules cites a minimum access standard of 1 Hz/s for 1 s, which is used in this paper.

In addition, the parameter D_p of the VSG is designed based on

$$D_p = \frac{1}{m_p}, \tag{4}$$

where

$$m_p = \frac{2\pi(f_{max} - f_{min})}{2 \times P_{max}} \tag{5}$$

is the frequency droop coefficient considering that the VSG is capable to supply and absorb active power (i.e., the VSG interfaces large-scale battery storage systems, where the batteries can be charged and discharged) [24]. f_{max} and f_{min} are the maximum and minimum frequency deviations, respectively, allowed in the IM. In addition, P_{max} is the maximum active power that can be supplied by the VSG.

Based on (2) and (3), J can be calculate as

$$J = T_{VSG}\frac{D_p}{\omega_0}. \tag{6}$$

By considering the VSG parameters shown in Table I, the initial ROCOF as 1 Hz/s (i.e., $T_{VSG} = 1$ s), and D_p as 1.273×10^6 W/Hz, J can be calculated as $J = 1 \times \frac{1.273\times10^6}{314.16} = 4053$ kg·m^2 based on (6).

Fig. 2 shows the VSG performance in the IM. Fig. 2(a) shows the VSG response to a step change of the load active power from 0 to 4 MW at $t = 0$ s, indicating that the initial ROCOF is equal to 0.5 Hz/s which is exactly the same as the designed value. Note that the designed ROCOF is equal to 1 Hz/s for the change of the active power from -4 MW to 4 MW. Fig. 2(b) presents the Bode plot of the open-loop transfer function of the VSG $G_p(s)$ which is calculated as

$$G_p(s) = \frac{\delta}{\Delta P_{\text{load}}} = \frac{1}{s(J\omega_0 s + D_p)}. \tag{7}$$

Fig. 2(c) presents the pole-zero plots of transfer function $\Delta\omega/\Delta P_{\text{load}}$. It can be seen that the VSG is a first-order system with a real negative pole. This pole contributes to the slow dynamic response (e.g., a longer settling time compared to that of the droop control) of the VSG, since it is very close to the imaginary axis [9].

The Q-V droop coefficient K_{pq} is calculated as

$$K_{pq} = \frac{(V_{\max} - V_{\min})}{2 \times Q_{max}}, \tag{8}$$

where $V_{\max}$ and $V_{\max}$ are the allowed maximum and minimum voltage deviations, respectively, specified by the grid code. In addition, Q_{max} is the maximum reactive power that can be supplied by the VSG. The number 2 in denominator indicates that the VSG is capable to supply and absorb reactive power. In the GCM, it is recommended to add an integral term K_{iq} to the reactive power controller K_{pq} in order to track the reactive power reference with zero steady-state error. Therefore, a PI controller is used in this paper for the reactive power control channel.

C. Control of the Conventional VSG in the GCM

In the GCM, the main control objective of the VSG is to regulate its output active and reactive power to the desired reference commands. To further investigate the performance of the VSG in the GCM and how the grid impedance parameter affects its performance, a small-signal model that considers the inherent power flow coupling is derived below, based on which the stability analysis is further investigated.

1) Power Flow Analysis and Small-Signal Modeling of the VSG in the GCM: Considering Fig. 1, the active and reactive power injected by the VSG to the grid can be calculated as

$$P_{\text{pcc}} = \frac{3}{R_{\text{g}}^2 + X_{\text{g}}^2}[R_{\text{g}}(V_i^2 - V_i V_j \cos\theta_{ij}) + X_{\text{g}} V_i V_j \sin\theta_{ij}], \tag{9}$$

and

$$Q_{\text{pcc}} = \frac{3}{R_{\text{g}}^2 + X_{\text{g}}^2}[X_{\text{g}}(V_i^2 - V_i V_j \cos\theta_{ij}) - R_{\text{g}} V_i V_j \sin\theta_{ij}], \tag{10}$$

respectively, where V_i and V_j are the RMS values of the grid voltages at the PCC and the grid-side (AC bus), respectively. R_{g} and X_{g} are the grid resistance and inductance, respectively. In addition, θ_{ij} is the phase angle between V_i and V_j.

To study the stability feature and dynamic performance of the VSG, the small-signal model of (9) and (10) is established as

$$\begin{bmatrix}\Delta P_{\text{pcc}} \\ \Delta Q_{\text{pcc}}\end{bmatrix} = \begin{bmatrix}K_{11} & K_{12} \\ K_{21} & K_{22}\end{bmatrix}\begin{bmatrix}\Delta\theta_{ij} \\ \Delta V_i\end{bmatrix}, \tag{11}$$

where K_{11}, K_{22}, K_{21}, and K_{22} are related to the specific operating point (θ_{ij0}, V_{i0}), shown as

$$\begin{cases} K_{11} = \dfrac{3}{R_{\text{g}}^2 + X_{\text{g}}^2}[R_{\text{g}} V_{i0} V_j \sin\theta_{ij0} + X_{\text{g}} V_{i0} V_j \cos\theta_{ij0}] \\ K_{12} = \dfrac{3}{R_{\text{g}}^2 + X_{\text{g}}^2}[R_{\text{g}}(2V_{i0} - V_j\cos\theta_{ij0}) + X_{\text{g}} V_j \sin\theta_{ij0}] \\ K_{21} = \dfrac{3}{R_{\text{g}}^2 + X_{\text{g}}^2}[X_{\text{g}} V_{i0} V_j \sin\theta_{ij0} - R_{\text{g}} V_{i0} V_j \cos\theta_{ij0}] \\ K_{22} = \dfrac{3}{R_{\text{g}}^2 + X_{\text{g}}^2}[X_{\text{g}}(2V_{i0} - V_j\cos\theta_{ij0}) - R_{\text{g}} V_j \sin\theta_{ij0}], \end{cases} \tag{12}$$

where 0 denotes the steady-state operating point. V_{i0} is the steady-state RMS value of the PCC line-to-ground voltage. θ_{ij0} is the power angle at the steady-state point.

Fig. 3 shows the small-signal model of the VSG in a resistive-inductive grid. It can be observed that the active and reactive power are coupled via the power angle and voltage magnitude, as presented in (9)-(12). In addition, the grid/line impedance (i.e., R_{g} and X_{g}) has a significant impact on both the coupling and direct-through terms. In summary, the independent control of active and reactive power is impossible in resistive-inductive grids. Therefore, such inherent coupling between the active and reactive power will hinder the optimal control of the VSG [11], [13].

2) The VSG Performance in the GCM: In Section II-B, the VSG parameters are designed based on the rated power and the ROCOF requirement in the IM. In this section, the VSG performance with the same parameters is tested in the GCM in order to illustrate the shortcoming if the fixed parameters of the VSG are used in the GCM.

Three test cases are conducted, which are the grid strength SCR variation, the $X_{\text{g}}/R_{\text{g}}$ ratio variation, and the Z_{g} variation with $X_{\text{g}}/R_{\text{g}}$ ratio unchanged. In all test cases, the VSG is operated at unit power factor, i.e., Q_{ref} = 0 MVar.

Fig. 4(a) and (b) show the simulation results of the VSG step responses under different SCR values as the $X_{\text{g}}/R_{\text{g}}$ is 3.0 and 1.0, respectively. It can be seen that the grid SCR significantly affects the VSG performance. Specifically, the step responses deteriorate in terms of overshoot, settling time, and oscillations under strong grid. In addition, the VSG performance is further deteriorated in all strong, weak, and very weak grids with

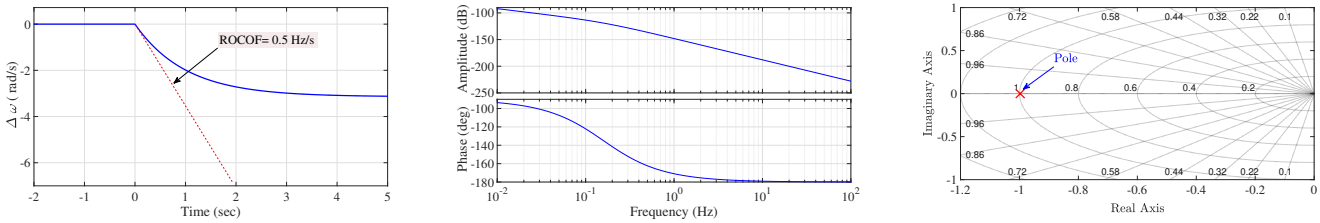

(a) **(b)** **(c)**

Fig. 2: VSG performance in the IM. (a) Step response of the $\Delta\omega$ as a 4 MW load power changes. (b) Bode plot of the transfer function $G_p(s)$ of the VSG. (c) The pole distribution of $\Delta\omega/\Delta P_{\text{load}}$.

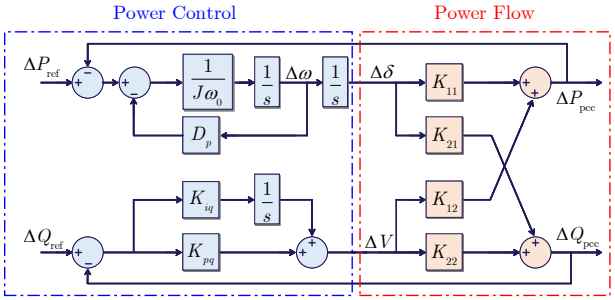

Fig. 3: Small-signal model of the VSG in the resistive-inductive grid.

smaller $X_{\text{g}}/R_{\text{g}}$ ratios as shown in Fig. 4(b), where $X_{\text{g}}/R_{\text{g}}$ is set as 1.0. Fig. 4(c) and (d) illustrate further the effects of the grid impedance on the VSG performance. It can be seen that the VSG performance deteriorates when connected to grids with small $X_{\text{g}}/R_{\text{g}}$ ratios. However, the effects of varying $X_{\text{g}}/R_{\text{g}}$ are much smaller compared with those of varying the grid SCR. Additionally, increasing the grid impedance amplitude while keeping the $X_{\text{g}}/R_{\text{g}}$ = 3 ratio unchanged results in significant impacts on the step response of the VSG active power output.

To further explain the effects of the grid conditions on the VSG performance, Fig. 5 presents the Bode plots for the test cases presented in Fig. 4. Note that the reactive power command is set to zero, so K_{12} and K_{22} are not considered in the analysis. In addition, K_{11} and K_{21} are obtained based on the linearized small-signal model of the power flow shown in (12), which are calculated from the steady-state operation of the VSG. The open-loop transfer functions of the active power loop considering both K_{11} and K_{21} can then be calculated as

$$\begin{cases} G_{11-\text{OL}}(s) = \dfrac{\Delta P_{\text{pcc}}}{\Delta P_{\text{ref}}} = \dfrac{1}{s(J\omega_0 s + D_p)} \times K_{11} \\ G_{21-\text{OL}}(s) = \dfrac{\Delta Q_{\text{pcc}}}{\Delta P_{\text{ref}}} = \dfrac{1}{s(J\omega_0 s + D_p)} \times K_{21}. \end{cases} \tag{13}$$

Fig. 5(a) and (e) presents the Bode plot of the VSG at two operating points, i.e., P_{ref} = 2 MW and 4 MW. It can be observed that operating point variation of the VSG has slight effects on the $G_{11-\text{OL}}(s)$ and $G_{21-\text{OL}}(s)$. However, the grid strength and the $X_{\text{g}}/R_{\text{g}}$ ratio variations have obvious effects on the VSG transfer functions $G_{11-\text{OL}}(s)$ and $G_{21-\text{OL}}(s)$.

D. Summary of the VSG Control Challenges in GCM

In Sections II-B and Section II-C, it is shown that the VSG cannot meet the desired performance in both the IM and GCM. In the IM, the VSG parameters have to be designed according to several constrains such as the rated active power and the ROCOF rule to avoid sharp increase or decrease in the frequency response when loads are disconnected or connected. In the GCM, the VSG has poor dynamic response due to the significant oscillations, long settling times, and the high overshoots. Such poor performance is related to the grid conditions such as the grid strength SCRs, $X_{\text{g}}/R_{\text{g}}$ ratio, and variation of Z_{g} with the same $X_{\text{g}}/R_{\text{g}}$ ratio. For example, the VSG performance is worsened further in strong-grid conditions.

Given the above analysis, it can be concluded that there is an inherent trade-off between meeting the ROCOF requirements in the IM and the fast and robust power regulation in the GCM, which prevents accurate control of the VSG with assigned fixed values for its control parameters. Hence, an adaptive VSG control strategy that takes the grid parameters into account may be a promising solution, as will be presented in the next section.

III. Proposed Adaptive Control of VSG

Fig. 6 and Fig. 7 show the control structure and the detailed implementation of the proposed AVSG control strategy. The control structure is very similar to the conventional VSG presented in Fig. 1. However, the control parameters D_p, J, K_{pq}, and K_{iq} of the AVSG are adaptively tuned online in order to achieve the reliable operation against the grid impedance variation. The tuning procedure is established based on the small-signal model of the power flow. Hence, it requires the grid impedance value, which is estimated online by the inverter itself. Further illustration on the proposed AVSG is provided next.

A. Adaptive Tuning Strategy for the VSG

The small-signal model of the VSG-grid system introduced in (11) and (12) is employed to obtain the relation between the VSG controller parameters and the system response. On its basis, the VSG controller parameters are tuned in an adaptive manner in order to have the desired response. $G_p(s)$ and $G_q(s)$ are defined as the transfer functions of the VSG and the reactive power controller in Fig. 3, i.e.,

$$G_p(s) = \frac{1}{s(J\omega_0 s + D_p)} \tag{14}$$

and

$$G_q(s) = K_{pq} + \frac{K_{iq}}{s}, \tag{15}$$

respectively. According to Fig. 3, the relation among $\Delta\theta_{ij}$, ΔV_i, ΔP_{ref}, and ΔQ_{ref} can be written as

$$\Delta\theta_{ij} = G_p(s)(\Delta P_{\text{ref}} - K_{11}\Delta\theta_{ij} - K_{12}\Delta V_i), \tag{16}$$

and

$$\Delta V_i = G_q(s)(\Delta Q_{\text{ref}} - K_{21}\Delta\theta_{ij} - K_{22}\Delta V_i), \tag{17}$$

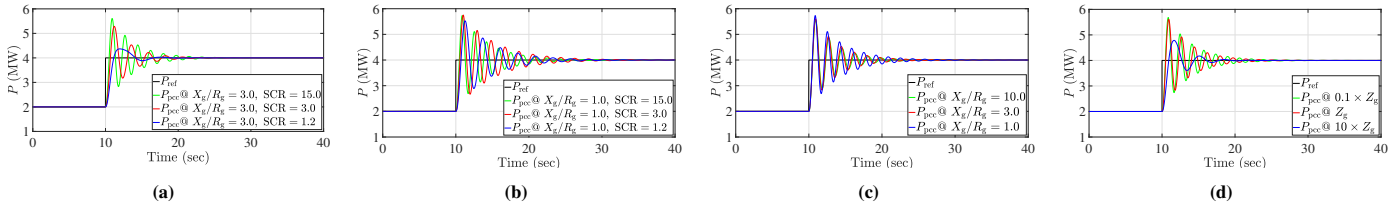

Fig. 4: VSG performance in GCM upon change in the active power reference form 2 MW to 4 MW where the J and D_p are kept constant and equal to the designed values in Subsection II-B: (a) Effects of SCR parameter when X_g/R_g = 3.0, (b) Effects of SCR parameter when X_g/R_g = 1.0, (c) Effects of X_g/R_g parameter when SCR = 15.0, (d) Effects of variation of Z_g for X_g/R_g=3.0.

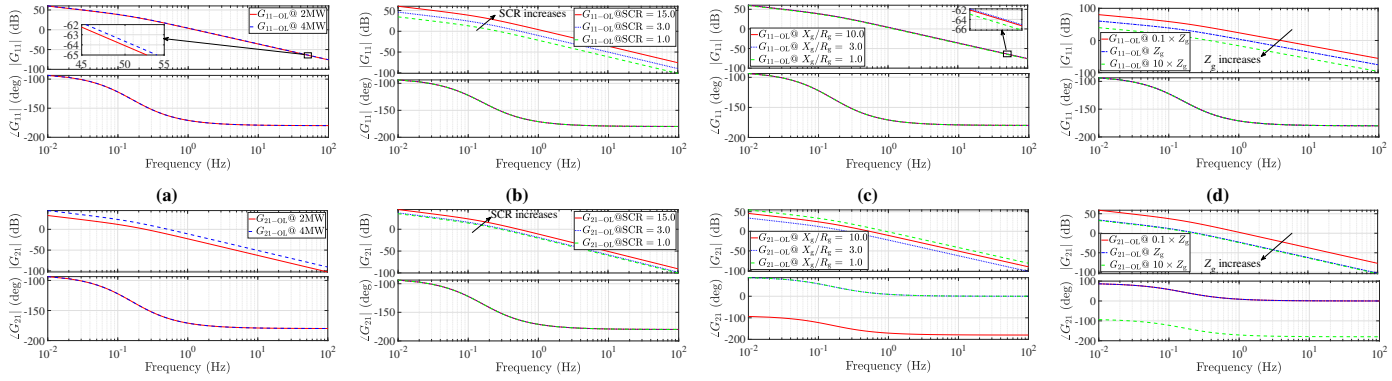

Fig. 5: The VSG performance in the GCM under Q_{ref} = 0 MVar and different scenarios for operating point and grid impedance: (a), (e) At two different operating points P_{ref} = 2 MW and 4 MW for same SCR= 15.0, and X_g/R_g = 3.0; (b), (f) Effects of the SCR when P_{ref} = 4 MW and Q_{ref} = 0 MVar for same X_g/R_g = 3.0, (c), (g) Effects of the X_g/R_g when P_{ref} = 4 MW for same SCR = 15.0, (d), (h) Effects of variation of Z_g for same X_g/R_g=3.0 and P_{ref} = 4 MW and Q_{ref} = 0 MVar.

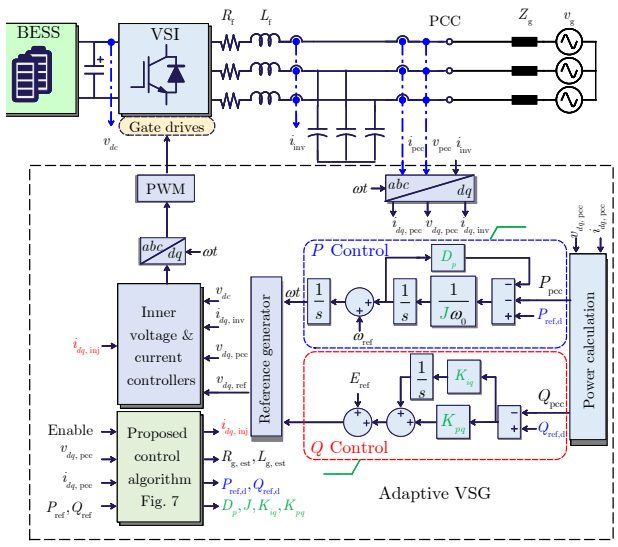

Fig. 6: Control structure of the proposed AVSG-based grid-forming inverters. The principle is relying the online GIE to tune the control parameters in order to cope with strong and weak grid conditions

which can be rearranged as

$$\begin{bmatrix}\Delta\theta_{ij}\\ \Delta V_i\end{bmatrix}=\begin{bmatrix}K_{11}G_p(s)+1 & K_{12}G_p(s)\\ K_{21}G_q(s) & K_{22}G_q(s)+1\end{bmatrix}^{-1}\begin{bmatrix}G_p(s)\Delta P_{\text{ref}}\\ G_q(s)\Delta Q_{\text{ref}}\end{bmatrix}. \tag{18}$$

By substituting (18) into (11), it can be derived that

$$\begin{bmatrix}\Delta P_{\text{pcc}}\\ \Delta Q_{\text{pcc}}\end{bmatrix}=\begin{bmatrix}H_{11} & H_{12}\\ H_{21} & H_{22}\end{bmatrix}\begin{bmatrix}\Delta P_{\text{ref}}\\ \Delta Q_{\text{ref}}\end{bmatrix}, \tag{19}$$

where

$$H_{11}(s)=\frac{G_p(s)(K_{11}+MG_q(s))}{1+K_{11}G_p(s)+K_{22}G_q(s)+MG_p(s)G_q(s)}, \tag{20}$$

$$H_{12}(s)=\frac{K_{12}G_q(s)}{1+K_{11}G_p(s)+K_{22}G_q(s)+MG_p(s)G_q(s)}, \tag{21}$$

$$H_{21}(s)=\frac{K_{21}G_p(s)}{1+K_{11}G_p(s)+K_{22}G_q(s)+MG_p(s)G_q(s)}, \tag{22}$$

and

$$H_{22}(s)=\frac{G_q(s)(K_{22}+MG_p(s))}{1+K_{11}G_p(s)+K_{22}G_q(s)+MG_p(s)G_q(s)}. \tag{23}$$

In addition, in (20) - (23),

$$M=K_{11}K_{22}-K_{12}K_{21}. \tag{24}$$

In order to have the desired dynamic response, assume that

$$H_{11}(s)=\frac{\omega_n^2}{s^2+2\zeta\omega_n s+\omega_n^2}, \tag{25}$$

i.e., $H_{11}(s)$ is a second-order transfer function with the natural frequency being ω_n and damping ratio being ζ. On the one hand, by replacing for $H_{11}(s)$ from (20) in (25) and then replacing for $G_p(s)$ and $G_q(s)$ from (14) and (15) in the obtained equation, one can have

$$\frac{\omega_n^2}{s(s+2\zeta\omega_n)}=\frac{1}{s(J\omega_0 s+D_p)}\frac{(MK_{pq}+K_{11})s+MK_{iq}}{(K_{22}K_{pq}+1)s+K_{22}K_{iq}}. \tag{26}$$

Having (26), the following conditions should be satisfied.

$$J\omega_0=\frac{MK_{pq}+K_{11}}{\omega_n^2(K_{22}K_{pq}+1)}, \tag{27}$$

$$D_p=\frac{MK_{iq}}{\omega_n^2(K_{22}K_{pq}+1)}, \tag{28}$$

$$K_{iq}=2\zeta\omega_n(K_{pq}+\frac{1}{K_{22}}). \tag{29}$$

On the other hand, by replacing for J, D_p, and K_{iq} from (27), (28), and (29) in (23), one can have

$$H_{22}(s)=\frac{\omega_n^2}{s^2+2\zeta\omega_n s+\omega_n^2}\frac{M+sK_{22}(J\omega_0 s+D_p)}{M+\frac{sK_{11}}{K_{pq}s+K_{iq}}}. \tag{30}$$

By defining

$$\sigma = 1 - \frac{M}{K_{11}K_{22}}, \tag{31}$$

and

$$\gamma = \frac{M(K_{22}K_{pq}+1)}{K_{22}(MK_{pq}+K_{11})}, \tag{32}$$

$H_{22}(s)$ can be rearranged as

$$H_{22}(s)=\frac{\gamma-1+\sigma}{\gamma\sigma}\frac{s+\frac{\gamma\sigma}{\gamma-1+\sigma}2\zeta\omega_n}{s+\gamma.2\zeta\omega_n}\frac{s^2+\gamma.2\zeta\omega_n s+\gamma\omega_n^2}{s^2+2\zeta\omega_n s+\omega_n^2}. \tag{33}$$

By selecting

$$K_{pq} = \frac{1}{K_{22}}, \tag{34}$$

It can be calculated that

$$\gamma = \frac{2-2\sigma}{2-\sigma}. \tag{35}$$

Thus, since the cross-coupling terms K_{12} and K_{21} are not dominant, i.e., $|K_{12}K_{21}| \leqslant |K_{11}K_{22}|$, it can be concluded from (31) that $0 \leqslant \sigma \leqslant 1$, and therefore, $0 \leqslant \gamma \leqslant 1$. As a result, in addition to a pair of poles which are similar to those of $H_{11}(s)$, $H_{22}(s)$ has a real pole and three zeros in the left-half plane and stable. Finally, by replacing (34) in (27), (28), and (29), one can have

$$J = \frac{2-\sigma}{2\omega_0}\frac{K_{11}}{\omega_n^2}, \tag{36}$$

$$D_p = \frac{2\zeta(1-\sigma)K_{11}}{\omega_n}, \tag{37}$$

and

$$K_{iq} = \frac{4\zeta\omega_n}{K_{22}}. \tag{38}$$

Based on (34), (36), (37), and (38), the VSG and the reactive power controller can be tuned such that $H_{11}(s)$ and $H_{22}(s)$ have the desired responses with the desired natural frequency ω_n and damping ζ. However, as can be seen in these equations, J, D_p, K_{pq}, and K_{iq} are functions of K_{11} and K_{22} which are further determined by the operating point, i.e., R_g, X_g, V_{i0}, V_j, and θ_{ij0}.

B. Online Event-based Grid Impedance Estimation Algorithm

It is demonstrated above that in order to tune the VSG to cope with both strong and weak grids, the grid impedance information should be known in advance. However, one key challenge is that the grid impedance is time-varying, which hinders the optimal design if only fixed values for the the grid impedance are used. Hence, accurate control can be only designed based on the actual value of the grid impedance. To solve this issue, the online GIE algorithms that make use of the inverter itself can be used [25]. This approach is cost effective as it does not require extra hardware, and uses only the available local measurements to estimate the grid impedance seen by the inverter at the PCC.

Several online GIE algorithms can be integrated into the control loop of the inverter itself. These algorithms are categorised generally into three groups, i.e., active, passive, and hybrid techniques [25]. The GIE techniques based on single frequency injection are shown to provide very accurate results if its estimation time and disturbance amplitude are designed properly [26]. Therefore, the online active GIE based on 75 Hz injection is chosen in this paper [27]. To avoid estimation errors related to the presence of background inter/sub-harmonics in the grid voltage, the injection/estimation time is set for 200 ms [26]. This permits accurate measuring due to the use of 5 Hz resolutions as per "Interharmonics – Recommended Updates to IEEE 519" [28].

To address the impacts of the perturbation currents on power quality and the trade-off between active and passive techniques, this paper proposes a new algorithm to automatically trigger the grid impedance only when it is required. Hence, possible adverse impacts of disturbance amplitude on power quality can significantly reduced [29], [30]. Additionally, to ensure a fast and accurate estimation of the grid impedance, the perturbation currents (i_{d-inj} and i_{q-inj}) are generated in the dq reference frame at 25 Hz and added to the current references i_{d-ref} and i_{q-ref} allowing fast tracking of the perturbation currents due to fast response of the inner loop.

Simultaneously with the injection of i_{d-inj} and i_{q-inj}, the current and voltage responses ($v_\mathrm{res}(75\ \mathrm{Hz})$, $i_\mathrm{res}(75\ \mathrm{Hz})$) at the PCC of phase A, B or C are recorded. Then, the fundamental grid impedance ($Z_\mathrm{g}(50\ \mathrm{Hz})$) is estimated by approximating its value to $Z_\mathrm{g}(75\ \mathrm{Hz})$ as shown in (39) [26], [27].

$$R_\mathrm{g} \cong \Re\left[\frac{v_\mathrm{res}(75\ \mathrm{Hz})}{i_\mathrm{res}(75\ \mathrm{Hz})}\right], \quad L_\mathrm{g} \cong \frac{1}{\omega_0}\Im\left[\frac{v_\mathrm{res}(75\ \mathrm{Hz})}{i_\mathrm{res}(75\ \mathrm{Hz})}\right] \tag{39}$$

C. Online Implementation of the Proposed AVSG

Fig. 7 shows in detail the online implementation of the proposed AVSG algorithm including the GIE algorithm and the adaptive tuning of the VSG. The proposed algorithm is summarized below:

1) Once the inverter is started, the control parameters designed by (4), (6) and (8) are used if the inverter is operating in the IM or in the GCM and the proposed AVSG is disabled.
2) Once the AVSG is enabled, the GIE algorithm is enabled to initialize the values of the impedance components R_g and X_g are being used in the next to calculate the linearized terms of the power flow shown in (12).
3) The control parameters J, D_p, K_{pq}, and K_{iq} of the VSG-based inverter are calculated based on the method proposed in (36), (37), (34), and (38), respectively. So, the inverter can now connect to the grid and the desired response with the desired natural frequency and damping is ensured.
4) Afterwards, the inverter power reference commands are read and monitored continuously for any changes. So, an enabling signal is generated each time the power reference commands are changed.
5) The enabling signal is used to delay the power reference commands for a time duration equal to the required time for the GIE algorithm, 200 ms. Simultaneously, the grid impedance parameters are estimated again in real-time to ensure reliable monitoring of the grid impedance variations.
6) Then, the updated impedance values are used to re-calculate J, D_p, K_{pq} and K_{iq}. By doing so, the inverter can cope with both strong and weak grid conditions as the effects of the grid impedance are resolved in real-time by the adaptive tuning of the control parameters of the inverter.

IV. Simulation and Experimental Results

A. Simulation Results

To evaluate the performance of the proposed AVSG and the conventional VSG, the system shown in Fig. 6 is simulated

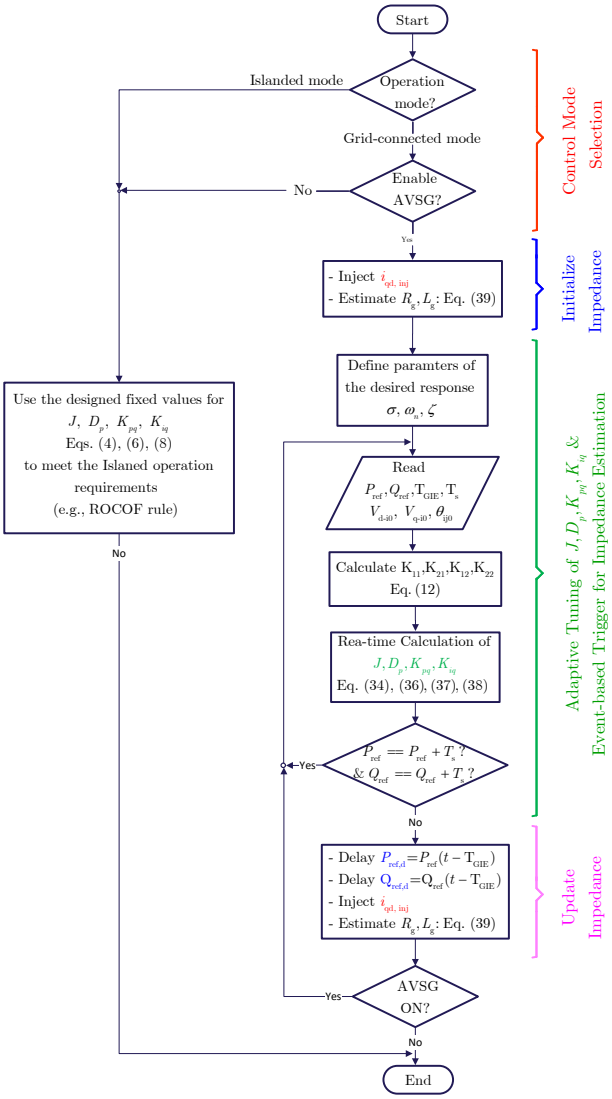

Fig. 7: Flow chart of the Proposed AVSG.

in MATLAB/Simulink and PLECS toolbox. The simulation parameters are listed in Table. I. The investigated test cases include active and reactive reference command changes for both weak and strong grid conditions. For each grid condition with the same SCR, different tests are conducted considering two different X/R ratios.

1) Strong Grid with $SCR = 8.0$: In this part, the performance of the AVSG is compared with that of the conventional VSG for strong grid conditions with two X_g/R_g ratios. For the X_g/R_g =5, grid impedance parameters are chosen as R_g =2.3 mΩ and L_g =37.1 μH. To simulate a strong grid with X_g/R_g =7, the grid impedance parameters are set to R_g =1.68 mΩ and L_g =37.5 μH.

The obtained results are shown in Fig. 8. Initially, the inverter active and reactive power reference commands are set to 0 MW and 0 Var. The AVSG controller is enabled at t =5 s. At t = 10 s, the inverter active power reference command changes from 0 to 2 MW. Then, it changes at t = 25 s to 4 MW. Finally, the reactive power reference command changes from 0 to 1.5 MVar. Fig. 8(a) and Fig. 8(d) show the dq components of the PCC voltage for both the VSG and AVSG corresponding to X_g/R_g =7 and X_g/R_g =5, respectively. Overall, it can be seen that the AVSG ensures seamless transient performance, without oscillations with a settling time around 0.8 s.

Additionally, as shown in Fig. 8(b) and Fig. 8(e), the dq components of PCC current change within the desired system

TABLE I: Parameters of the study system.

Quantity	Value	Unit	Description
Grid parameters			
v_g	690	V	Grid voltage (L-L)
f	50	Hz	Nominal frequency
Grid parameters (R_g, X_g) used for the comparison study: Section II-C			
R_g, L_g	0.63, 20	mΩ, μH	Strong grid with SCR=15.0, X_g/R_g=10
R_g, L_g	2, 19	mΩ, μH	Strong grid with SCR=15.0, X_g/R_g=3
R_g, L_g	4.5, 14.3	mΩ, μH	Strong grid with SCR=15.0, X_g/R_g=1
R_g, L_g	10, 95.8	mΩ, μH	Weak grid with SCR=3.0, X_g/R_g=3
R_g, L_g	22.4, 71.4	mΩ, μH	Weak grid with SCR=3.0, X_g/R_g=1
R_g, L_g	25, 239.6	mΩ, μH	Weak grid with SCR=1.0, X_g/R_g=3
R_g, L_g	56, 178.6	mΩ, μH	Weak grid with SCR=1.0, X_g/R_g=1
Grid parameters (R_g, X_g) used for the simulation study: Section IV-A			
R_g, L_g	1.68, 37.5	mΩ, μH	Strong grid with SCR=8.0, X_g/R_g=7.0
R_g, L_g	2.3, 37.1	mΩ, μH	Strong grid with SCR=8.0, X_g/R_g=5.0
R_g, L_g	25, 239.6	mΩ, μH	Weak grid with SCR=1.2, X_g/R_g=3
R_g, L_g	56, 178.6	mΩ, μH	Weak grid with SCR=1.2, X_g/R_g=1
Inverter parameters			
S_{base}	5.0	MVA	Inverter rated power
P_{base}	5.0	MW	Inverter rated active power
v_{dc}	3000	V	DC Bus voltage
f_{sw}	5	kHz	Inverter PWM carrier fequency
L_f	95	μH	Filter inductance
R_f	0.01	Ω	Filter resistance
C_f	1	mF	Filter capacitance
Fixed parameters for the conventional VSG			
D_p	1.273×10^6	W/Hz	Damping coefficient
J	4052.85	kg.m^2	Inertia coefficient
K_{pq}	1.5×10^{-5}	Var/V	Proportional gain of reactive power controller
K_{iq}	1×10^{-3}	1/s	Integral gain of reactive power controller

response. The zoom-in view in Fig. 8(b) and Fig. 8(c) present the small variations in the dq current required to estimate the grid impedance in real-time. As stated previously, these small variations result from the injected 75 Hz perturbations in the dq current reference for a duration of t =200 ms.

Fig. 8(c) and Fig. 8(f) show robust performance of the AVSG in a strong grid against both X_g/R_g=7 and X_g/R_g=5. In contrast to the proposed AVSG, the conventional VSG shows unstable operation in the higher inductive grid X_g/R_g =7 after the reactive power reference command changes from 0 to 1.5 MVar while the inverter injects its rated active power of 4 MW.

2) Weak Grid with SCR = 1.2: Similar to the previous test in strong grid conditions, the grid impedance parameters are chosen to simulate two case studies for a weak grid with SCR = 1.2. In the first case study, the grid parameters are chosen as R_g =25.1 $m\Omega$ and L_g =239.61 μH to obtain X_g/R_g =3. In the second case study, the grid parameters are chosen as R_g =56.1 $m\Omega$ and L_g =178.6 μH to obtain X_g/R_g =1.

The simulated events of active and reactive power reference commands changes are similar to those reported in the previous section for strong grid tests. Fig. 9 shows that the AVSG outperforms the conventional VSG. It is evident that the AVSG is robust against the variations of the X_g/R_g = ratios.

Fig. 10 depicts the control signals, the PCC current, and the estimated grid impedance of the AVSG for the second case study with X_g/R_g=1. Fig. 10(a) shows that the GIE algorithm is activated four times at 5, 10, 25, and 40 s. Unlike the first activation of the GIE algorithm at t =5 s that corresponds to the time instance of enabling the AVSG, the GIE algorithm is enabled automatically at 10, 25 and 40 s due to changes of the inverter active and reactive reference commands. Fig. 10(a) also depicts the perturbation currents, i_{d-inj}, and i_{q-inj} required for the impedance estimation. It can be seen that the GIE algorithm has minimal impact on the system as it does not disrupt the system continuously and the injected perturbation currents have relatively small amplitudes of 3.3 A. Fig. 10(b) shows the PCC current with zoom-in view of the time duration when the GIE is enabled. Fig. 10(c) compares the estimated grid components (R_{est} and L_{est}) with their true/reference values. It is evident that the

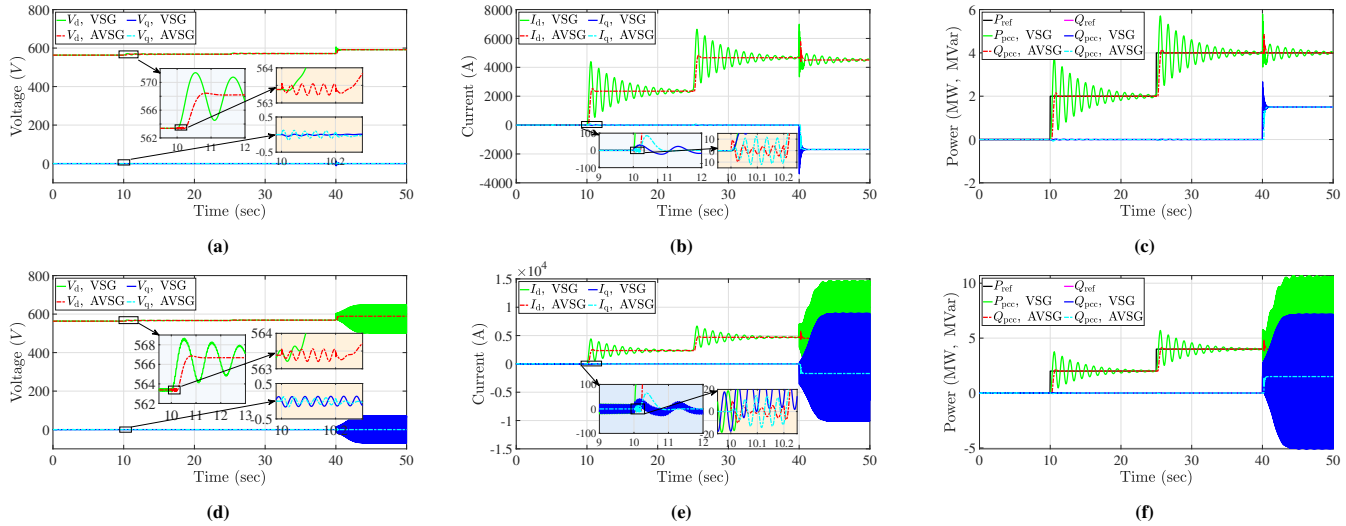

Fig. 8: The simulation results of the conventional VSG and the AVSG upon changes in the active and reactive power references when the inverter is connected to a strong grid SCR = 8.0 and: (a),(b) (c) for X_g/R_g = 5.0; and (d),(e) (f) for X_g/R_g = 7.0.

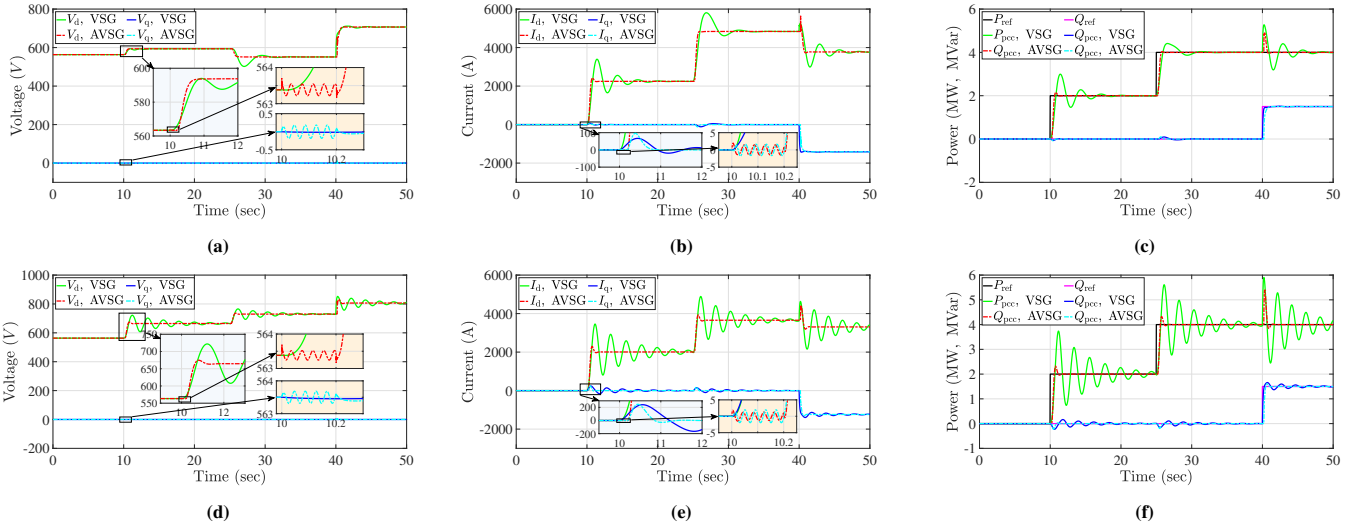

Fig. 9: Simulation results of the conventional VSG and the AVSG upon changes in the active and reactive power references when the inverter is connected to a weak grid SCR = 1.2 and: (a),(b) (c) for X_g/R_g = 3.0; and (d),(e) (f) for X_g/R_g = 1.0.

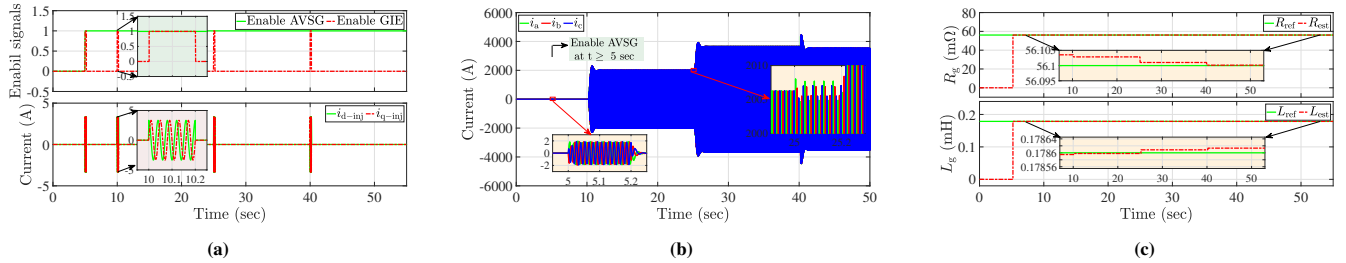

Fig. 10: The simulation results of the AVSG in a very weak grid (SCR= 1.2, X/R=1): (a) Enable Signal; and dq current injections for GIE; (b) PCC current; (c) References and estimated grid resistance and inductance.

proposed implementation of the GIE is reliable and provide very accurate results.

B. Experimental Results

In this section, the experimental results based on a scaled-down setup are presented to validate the effectiveness of the proposed control. The tested systems are the conventional VSG and the AVSG as presented in Fig. 1 and Fig. 6, respectively. The system parameters used for the experiment are listed Table. II. Fig. 11 shows the experimental setup used for evaluating the control performance. It consists of a DC power supply, a SiC-based two-level three-phase Imperix inverter, LC filter, grid impedance, and a Regatron grid simulator. The control algorithm was implemented directly from MATLAB/Simulink into the BoomBox Imperix Controller.

The performance of the controller is tested in both strong and weak grids. In each test, step changes in the active and reactive power reference commands are applied. Initially, both inverters are operating in steady state where the power reference commands are $P_{\text{ref}} = 200$ W and $Q_{\text{ref}} = 0$ Var. Then, for the proposed AVSG, the control algorithm is enabled at t_1 and the values of $i_{\text{d-inj}}$ and $i_{\text{q-inj}}$ are set to 0.25 A. After 5 s of enabling the AVSG, a step change in the active power

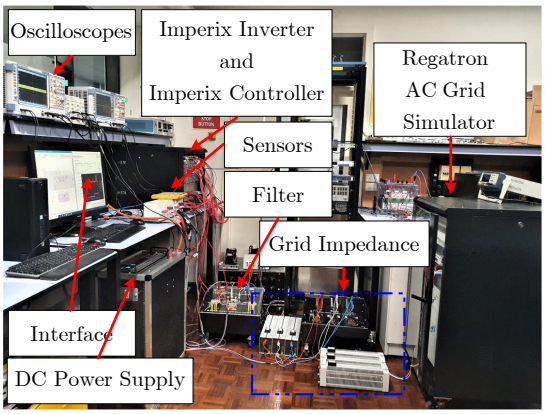

Fig. 11: The experimental setup.

TABLE II: Parameters of the experimental setup.

Quantity	Value	Unit	Description
Grid parameters			
v_g	110	V	Grid voltage (L-L)
f	50	Hz	Nominal frequency
R_g, L_g	0.85, 3.0	mΩ, μH	Strong grid with SCR=6.74, X_g/R_g=1.1
R_g, L_g	0.67, 10.5	mΩ, μH	Weak grid with SCR=2.54, X_g/R_g=4.92
Inverter parameters			
S_{base}	1.4142	kVA	Inverter rated power
P_{base}	1.0	kW	Inverter rated active power
v_{dc}	320	V	DC Bus voltage
f_{sw}	5	kHz	Inverter PWM carrier fequency
L_f	4	mH	Filter inductance
R_f	0.06	Ω	Filter resistance
C_f	30	μF	Filter capacitance
Fixed parameters for the conventional VSG			
D_p	318.3	W/Hz	Damping coefficient
J	1.013	kg.m^2	Inertia coefficient
K_{pq}	7.18× 10^{-3}	Var/V	Proportional gain of reactive power controller
K_{iq}	1× 10^{-5}	1/s	Integral gain of reactive power controller

reference command from 200 to 800 W is applied at t_2. Finally, a step change in the reactive power reference command from 0 to 150 Var is applied at t_3.

Fig. 12 shows the experimental results in a strong grid. Fig. 12(a) and Fig. 12(b) compare the PCC currents and the power tracking capability of the VSG and the proposed AVSG, respectively. It is evident that there are significant oscillations in the output power waveform of the conventional VSG for almost 10 s. In contrast, the AVSG ensures good dynamic performance. After the changes of active power reference command, the AVSG takes an overall t =1 s to settle down (0.2 s for the GIE and 0.8 s for tracking the new power reference commands).

Similarly, Fig. 13 shows the experimental results in a weak grid. Fig. 13(a) and Fig. 13(b) compare the PCC currents and the power tracking capability of the VSG and the proposed AVSG, respectively. It can be observed that the proposed AVSG ensures the seamless transient in a weak grid. It requires a time duration equal to 1 s to settle down, as the same desired performance obtained for the strong grid condition. In contrast, the VSG has poor dynamic performance in a weak grid due to the large grid inductance, but still performs better than in a strong grid.

In summary, this paper proposes an adaptive control for VSG-based inverters. The proposed AVSG ensures good dynamic performance in both strong and weak grid conditions. It is robust against grid impedance variations and with different g/R_g values as it relies on the online estimation of the grid impedance.

V. Conclusions

This paper initially reveals the negative impacts of grid parameters (SCR, X_g/R_g ratios, and different amplitudes of

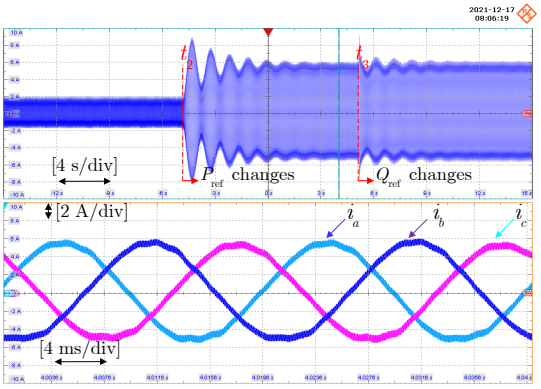

(a)

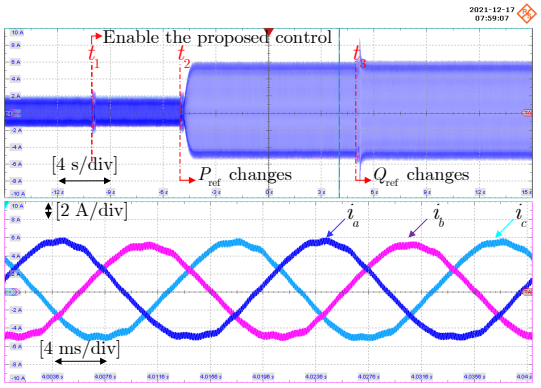

(b)

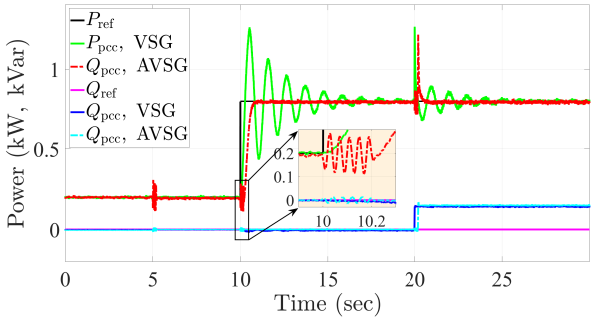

(c)

Fig. 12: The experimental results of the conventional and the AVSG in a strong grid (SCR=6.74, X_g/R_g=1.1): (a) PCC current waveforms of the conventional VSG, (b) PCC current waveforms of the proposed AVSG, (c) PCC power waveforms.

the grid impedance) on the performance of the VSG. Then, an online grid impedance estimation-based adaptive control strategy is proposed to ensure the full decoupling of the active and reactive power flow. This technique ensures full control of the real and reactive powers with the same desired dynamic performance, such as no oscillation, specified time duration for the settling time, and minimal overshoot, regardless of the grid parameters. The proposed control is established based on the online estimation of the grid impedance using the frequency injection estimation algorithm that is embedded into the control loop of the AVSG-based inverter. Furthermore, to avoid the unnecessary continuous estimation of the grid impedance, the estimation algorithm is automated to re-estimate the grid impedance only if the active or reactive power reference commands are changed. Simulation and experimental results validated the efficacy of the proposed online grid impedance estimation-based adaptive control for VSGs in both strong and weak grid conditions.

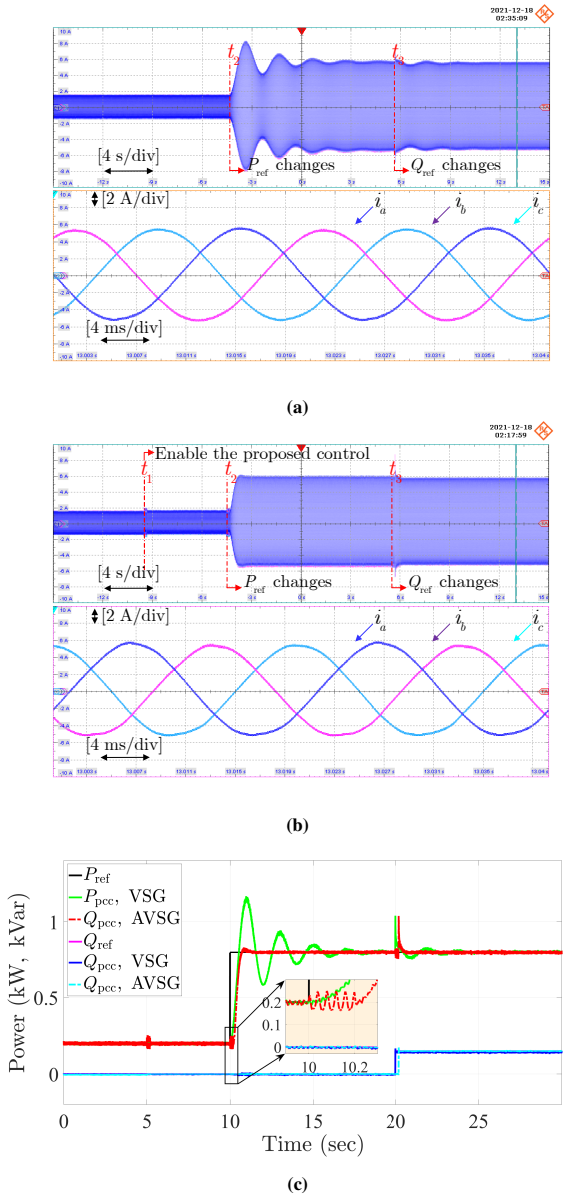

Fig. 13: The experimental results of the conventional and the AVSG in a weak grid (SCR=2.54, X_g/R_g=4.92): (a) PCC current waveforms of the conventional VSG, (b) PCC current waveforms of the proposed AVSG, (c) PCC power waveforms.

REFERENCES

[1] R. Secretariat, "Renewables 2020 global status report," *Rep. Paris: REN12*, 2020.

[2] Q.-C. Zhong, "Power-electronics-enabled autonomous power systems: Architecture and technical routes," *IEEE Transactions on Industrial Electronics*, vol. 64, no. 7, pp. 5907–5918, 2017.

[3] X. Wang, M. G. Taul, H. Wu, Y. Liao, F. Blaabjerg, and L. Harnefors, "Grid-synchronization stability of converter-based resources—an overview," *IEEE Open Journal of Industry Applications*, vol. 1, pp. 115–134, 2020.

[4] W. Zhou, Y. Wang, R. E. Torres-Olguin, and Z. Chen, "Effect of reactive power characteristic of offshore wind power plant on low-frequency stability," *IEEE Transactions on Energy Conversion*, vol. 35, no. 2, pp. 837–853, 2020.

[5] W. Zhou, R. E. Torres-Olguin, Y. Wang, and Z. Chen, "Dq impedance-decoupled network model-based stability analysis of offshore wind power plant under weak grid conditions," *IET Power Electronics*, vol. 13, no. 13, pp. 2715–2729, 2020.

[6] R. H. Lasseter, Z. Chen, and D. Pattabiraman, "Grid-forming inverters: A critical asset for the power grid," *IEEE Journal of Emerging and Selected Topics in Power Electronics*, vol. 8, no. 2, pp. 925–935, 2019.

[7] D. B. Rathnayake, M. Akrami, C. Phurailatpam, S. P. Me, S. Hadavi, G. Jayasinghe, S. Zabihi, and B. Bahrani, "Grid forming inverter modeling, control, and applications," *IEEE Access*, 2021.

[8] K. M. Cheema, "A comprehensive review of virtual synchronous generator," *International Journal of Electrical Power & Energy Systems*, vol. 120, p. 106006, 2020.

[9] X. Meng, J. Liu, and Z. Liu, "A generalized droop control for grid-supporting inverter based on comparison between traditional droop control and virtual synchronous generator control," *IEEE Transactions on Power Electronics*, vol. 34, no. 6, pp. 5416–5438, 2018.

[10] M. Liserre, R. Cardenas, M. Molinas, and J. Rodriguez, "Overview of multi-mw wind turbines and wind parks," *IEEE Transactions on Industrial Electronics*, vol. 58, no. 4, pp. 1081–1095, 2011.

[11] T. Wen, D. Zhu, X. Zou, B. Jiang, L. Peng, and Y. Kang, "Power coupling mechanism analysis and improved decoupling control for virtual synchronous generator," *IEEE Transactions on Power Electronics*, vol. 36, no. 3, pp. 3028–3041, 2020.

[12] B. Li, L. Zhou, X. Yu, C. Zheng, and J. Liu, "Improved power decoupling control strategy based on virtual synchronous generator," *IET Power Electronics*, vol. 10, no. 4, pp. 462–470, 2017.

[13] M. Li, Y. Wang, W. Hu, S. Shu, P. Yu, Z. Zhang, and F. Blaabjerg, "Unified modeling and analysis of dynamic power coupling for grid-forming converters," *IEEE Transactions on Power Electronics*, vol. 37, no. 2, pp. 2321–2337, 2021.

[14] Y. Li and Y. W. Li, "Power management of inverter interfaced autonomous microgrid based on virtual frequency-voltage frame," *IEEE Transactions on Smart Grid*, vol. 2, no. 1, pp. 30–40, 2011.

[15] T. Wu, Z. Liu, J. Liu, S. Wang, and Z. You, "A unified virtual power decoupling method for droop-controlled parallel inverters in microgrids," *IEEE Transactions on Power Electronics*, vol. 31, no. 8, pp. 5587–5603, 2015.

[16] J. M. Guerrero, L. G. De Vicuna, J. Matas, M. Castilla, and J. Miret, "Output impedance design of parallel-connected ups inverters with wireless load-sharing control," *IEEE Transactions on industrial electronics*, vol. 52, no. 4, pp. 1126–1135, 2005.

[17] J. Matas, M. Castilla, L. G. de Vicuna, J. Miret, and J. C. Vasquez, "Virtual impedance loop for droop-controlled single-phase parallel inverters using a second-order general-integrator scheme," *IEEE Trans. Power Electron*, vol. 25, no. 12, pp. 2993–3002, 2010.

[18] H. Zhang, S. Kim, Q. Sun, and J. Zhou, "Distributed adaptive virtual impedance control for accurate reactive power sharing based on consensus control in microgrids," *IEEE Transactions on Smart Grid*, vol. 8, no. 4, pp. 1749–1761, 2016.

[19] J. C. Vasquez, J. M. Guerrero, A. Luna, P. Rodríguez, and R. Teodorescu, "Adaptive droop control applied to voltage-source inverters operating in grid-connected and islanded modes," *IEEE transactions on industrial electronics*, vol. 56, no. 10, pp. 4088–4096, 2009.

[20] U. B. Tayab, M. A. B. Roslan, L. J. Hwai, and M. Kashif, "A review of droop control techniques for microgrid," *Renewable and Sustainable Energy Reviews*, vol. 76, pp. 717–727, 2017.

[21] B. Li and L. Zhou, "Power decoupling method based on the diagonal compensating matrix for vsg-controlled parallel inverters in the microgrid," *Energies*, vol. 10, no. 12, p. 2159, 2017.

[22] T. Wen, X. Zou, D. Zhu, X. Guo, L. Peng, and Y. Kang, "Comprehensive perspective on virtual inductor for improved power decoupling of virtual synchronous generator control," *IET Renewable Power Generation*, vol. 14, no. 4, pp. 485–494, 2020.

[23] H. Wu, X. Ruan, D. Yang, X. Chen, W. Zhao, Z. Lv, and Q.-C. Zhong, "Small-signal modeling and parameters design for virtual synchronous generators," *IEEE Transactions on Industrial Electronics*, vol. 63, no. 7, pp. 4292–4303, 2016.

[24] J. M. Guerrero, M. Chandorkar, T.-L. Lee, and P. C. Loh, "Advanced control architectures for intelligent microgrids—part i: Decentralized and hierarchical control," *IEEE Transactions on Industrial Electronics*, vol. 60, no. 4, pp. 1254–1262, 2012.

[25] M. Ciobotaru, V. Agelidis, and R. Teodorescu, "Line impedance estimation using model based identification technique," in *Proceedings of the 2011 14th European Conference on Power Electronics and Applications*. IEEE, 2011, pp. 1–9.

[26] N. Mohammed, M. Ciobotaru, and G. Town, "Fundamental grid impedance estimation using grid-connected inverters: A comparison of two frequency-based estimation techniques," *IET Power Electronics*, vol. 13, no. 13, pp. 2730–2741, 2020.

[27] A. V. Timbus, R. Teodorescu, F. Blaabjerg, and U. Borup, "Online grid impedance measurement suitable for multiple pv inverters running in parallel," in *Twenty-First Annual IEEE Applied Power Electronics Conference and Exposition, 2006. APEC'06.* IEEE, 2006, pp. 5–pp.

[28] E. W. Gunther, "Interharmonics-recommended updates to ieee 519," in *IEEE Power Engineering Society Summer Meeting,*, vol. 2. IEEE, 2002, pp. 950–954.

[29] P. Garcia, M. Sumner, Á. Navarro-Rodríguez, J. M. Guerrero, and J. Garcia, "Observer-based pulsed signal injection for grid impedance estimation in three-phase systems," *IEEE Transactions on Industrial Electronics*, vol. 65, no. 10, pp. 7888–7899, 2018.

[30] N. Mohammed, T. Kerekes, and M. Ciobotaru, "An online event-based grid impedance estimation technique using grid-connected inverters," *IEEE Transactions on Power Electronics*, vol. 36, no. 5, pp. 6106–6117, 2020.